Components of Upper-Ocean Salt Transport by the Gyres and the Meridional Overturning Circulation

C. S. JONES

Lamont Doherty Earth Observatory, Columbia University, Palisades, New York

PAOLA CESSI

Scripps Institution of Oceanography, University of California, San Diego, San Diego, California

ABSTRACT

The salt transport by the wind-driven gyres and the meridional overturning circulation (MOC) is studied in an idealized-geometry primitive equation ocean model. Two narrow continents, running along meridians, divide the model domain into two basins of different widths connected by a re-entrant channel south of 52.5°S. One of the continents, representing the Americas, is longer than the other, representing Europe/Africa. Two different configurations of the model are used: the "standard" one, in which the short continent is west of the wide basin, and the "exchanged" one, in which the short continent is west of the narrow basin. In both cases, deep water is formed in the basin to the west of the short continent. Most residual transport of the MOC's upper branch enters this basin by flowing along open streamlines that pass westward south of the short continent before proceeding northward. The meridional salt transport in the upper ocean of the sinking basin is decomposed into two portions: transport along open streamlines and transport by closed streamlines (gyres). In the Northern Hemisphere of the basin in which deep water is formed, the total northward salt transport per unit width along open streamlines is larger in the standard configuration than in the exchanged configuration. This larger salt transport is caused by two factors: a larger northward advection of salt by the interbasin transport and a larger cross-streamline salt transport out of the subpolar gyre. It is concluded that increasing interbasin flow south of Africa would likely bring more salt into the Atlantic Ocean.

1. Introduction

The global meridional overturning circulation (MOC) is a key component of Earth's climate system, transporting heat northward at all latitudes in the Atlantic Ocean and regulating ocean uptake of carbon dioxide. In the current regime, Antarctic Intermediate Water (AAIW) is transported northward out of the Southern Ocean in the upper ocean. This AAIW contributes to deep-water formation in the North Atlantic, which is enabled by the high salinity (and density) there. North Atlantic Deep Water then spreads southward across the whole ocean and upwells in the Southern Ocean and Indo-Pacific Oceans, closing the MOC loop by returning to the North Atlantic as intermediate water (Lumpkin and Speer 2007). The return flow follows three pathways: the cold route via Drake Passage (Rintoul 1991), the warm route via the Indonesian Throughflow (ITF) (Gordon 1985), and the Tasman leakage (Speich et al. 2002). Water from the Tasman leakage and the ITF flows westward south of Africa, transporting warm salty water into the Atlantic via the Agulhas leakage, and reinforcing Atlantic sinking (Reid 1961; Gordon 1986; Nilsson et al. 2013). A supergyre spans the Atlantic, Indian, and Pacific Oceans, with western boundary currents in the Atlantic and Indian sectors (Speich et al. 2002; Ridgway and Dunn 2007). The cold route, the warm route, the Tasman leakage, the supergyre, and the Antarctic Circumpolar Current all exchange salt between the Atlantic and Indo-Pacific sectors. The partition of transport between the warm and cold routes is not well established because it is difficult to distinguish the interbasin flow through the Southern Ocean from the large Antarctic Circumpolar Current (ACC) transport (Rintoul 1991). The goal of this paper is to understand the partition of salt transport among various components of the interbasin salt exchange.

Corresponding author: C. S. Jones, spencerj@ldeo.columbia.edu

Observations suggest that the MOC transports salt into the Atlantic basin (Garzoli et al. 2013), possibly reinforcing deep-water formation in the North Atlantic (Rahmstorf 1996). In Cessi and Jones (2017) and Jones and Cessi (2017), we investigated how ocean basin geometry influences the location of deep-water formation. These papers used an ocean-only idealized model in which two narrow continents, running along meridians, divide the domain into two basins of different widths connected by a re-entrant channel south of 52.5°S. At the surface, this model is forced with a zonally uniform wind stress, temperature relaxation, and freshwater flux. The basin where deep water is formed (the sinking basin) represents the Atlantic and the other basin (the nonsinking basin) represents the Indo-Pacific. The interbasin transport returns upwelled water from the Indo-Pacific to the Atlantic. In this idealized model, when both continents end south of the zero wind stress curl line (which is at about 42°S), all of the interbasin transport follows the cold route, flowing into the sinking basin from the west. When both continents are the same length, there is a preference for narrow-basin sinking despite zonally uniform surface forcing. This preference is caused by the weaker subpolar gyre in the narrow basin, which allows the MOC's upper branch to transport salt northward more efficiently into the region where deep water is formed (Jones and Cessi 2017).

In addition to the preference for narrow-basin sinking, if one continent ends north of the zero wind stress curl line there is a preference for deep-water formation in the basin with the short eastern boundary. When the shorter continent ends at 21°S, the effect of continent length overwhelms the effect of basin width. All of the interbasin transport flows westward south of the shorter continent, proceeding northward into the sinking basin (Cessi and Jones 2017). The size of this interbasin transport is approximately proportional to the width of the nonsinking basin (Jones and Cessi 2016; Cessi and Jones 2017). In the work presented here, the size of the interbasin transport is changed by varying the width of the nonsinking basin (which is to the east of the short continent).

This paper seeks to understand the pathway of salt flowing into the north of the sinking basin. Specifically, we wish to quantify the amount of salt transported by the MOC's upper branch versus that transported by the gyres and to understand how this partition depends on the flow configuration. Our approach compares two idealized geometries of an ocean-only general circulation model. Using a pseudostreamfunction for the warm-route interbasin transport flow (described in section 2), the domain is broken into a region of open streamlines and a region of closed streamlines (gyres). In section 3, it is shown that the salt transport per unit width (p.u.w.) along open streamlines in the sinking basin is larger in the configuration with a larger interbasin transport. The width of the sinking basin also influences the salinity in the sinking region (section 4). A summary of our results is provided in section 5.

2. Methods

The numerical model employed is the Massachusetts Institute of Technology GCM (MITgcm; Marshall et al. 1997a,b), which integrates the hydrostatic, Boussinesq primitive equations. The domain is a spherical sector, spanning from −70° to 70° in latitude and covering 210° in longitude, with a horizontal resolution of 1°. The domain consists of two idealized basins of different widths, separated by "continents" one grid point wide aligned along meridians. At the southern edge, a periodic channel of minimum latitudinal width 17.5° connects the basins, as shown in Figs. 1a and 1b. The bottom is flat and 4000 m deep, except for a sill in the periodic channel, one grid point wide and 1333 m high, located immediately south of the narrow basin's western boundary. There are 32 unequally spaced levels in the vertical direction, ranging from a minimum spacing of 13.6 m at the top to a maximum of 286 m at the bottom.

The equation of state is linear, with the buoyancy described by

$$b = g[\alpha_T T - \beta_S (S - S_{\text{ref}})], \tag{1}$$

where $\alpha_T = 2 \times 10^{-4}$°C^{-1}, $\beta_S = 7.4 \times 10^{-4}$, and $S_{\text{ref}} = 35$. Salinity is given on the practical salinity scale and is therefore presented without units. Temperature is in Celsius.

The model is forced at the surface by zonally uniform wind stress τ, freshwater flux F, and temperature relaxation to a profile T^*, respectively given by

$$\tau = \tau_{\max}[-\cos(3\pi\theta/140) + e^{-\theta^2/\sigma^2}], \tag{2}$$

$$F = F_s[\cos(7\pi\theta/8\Theta) - 2e^{-(\theta/\Theta)^2/(2\sigma_F^2)}] - F_0, \quad \text{and} \tag{3}$$

$$T^* = T_{\text{eq}}[\cos(\pi\theta/140)^2 + 0.1e^{-(\theta/2\Theta-1)^2}], \tag{4}$$

where θ is latitude in degrees, $\tau_{\max} = 0.1$ N m^{-2}, $\sigma = 10°$, $F_s = 2 \times 10^{-8}$ m s^{-1}, $\sigma_F = 0.128$, $\Theta = 60°$, and $T_{\text{eq}} = 25$°C (see Figs. 1c–e). The relaxation time scale for the surface temperature is 10 days. The freshwater flux is multiplied by the negative reference salinity $-S_{\text{ref}}$ to obtain the salt flux into the ocean. The constant F_0 is chosen so that the net freshwater flux into the ocean is zero. Thus, the average salinity of the ocean remains constant at $S_{\text{ref}} = 35$.
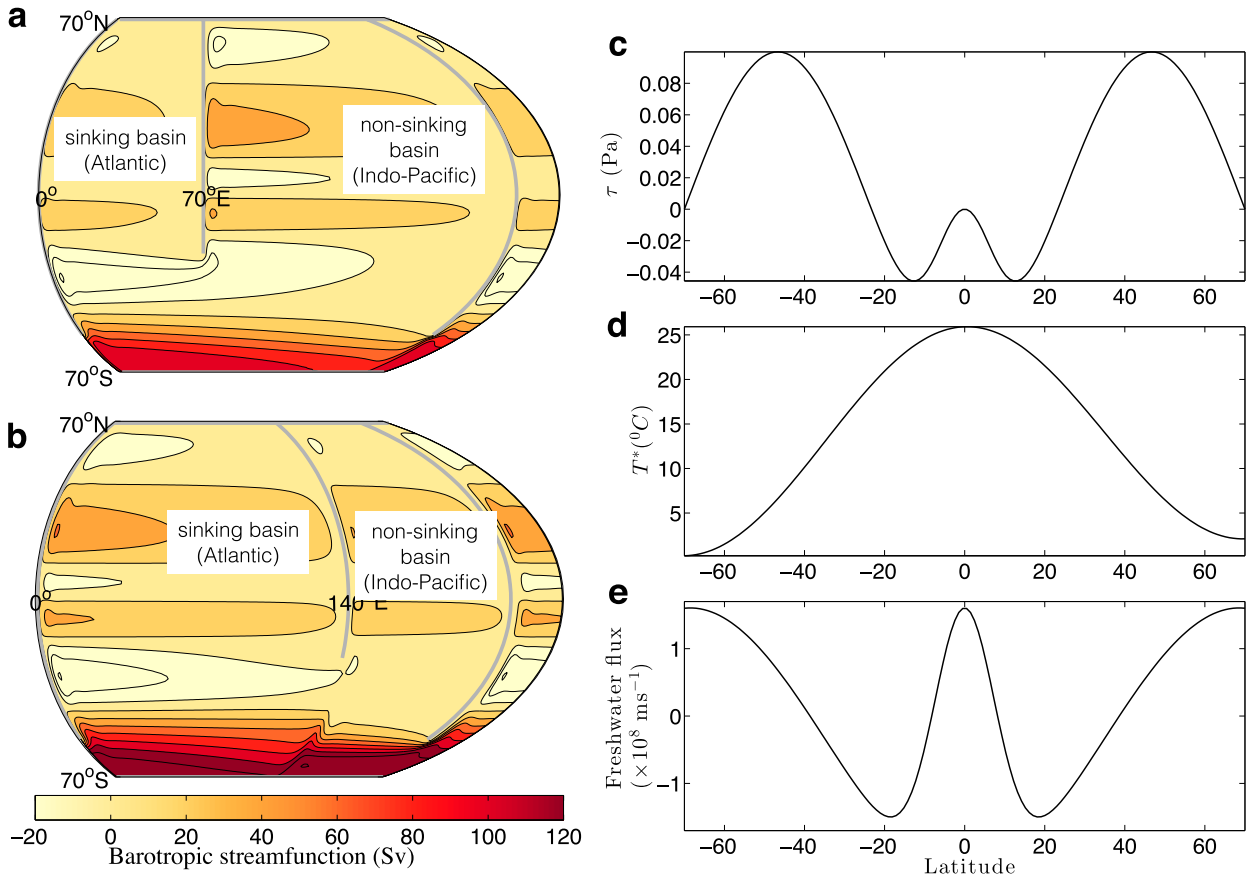
FIG. 1. The barotropic streamfunction in the geometry of (a) the standard configuration and (b) the exchanged configuration. The gray lines indicate solid boundaries. The domain is 140° in latitude, 210° periodic in longitude, and 4000 m deep. The westernmost 20° of the domain is repeated on the right side of the panels. In both cases, deep water is formed in the basin to the west of the short continent. Also shown are (c) surface wind stress (Pa), (d) the profile of temperature used for temperature relaxation (°C), and (e) surface freshwater flux forcing ($\times 10^8 \, \mathrm{m \, s^{-1}}$).

Baroclinic eddies are parameterized using the Gent–McWilliams advective form (Gent and McWilliams 1990) and the Redi (1982) isopycnal tracer mixing with equal mixing coefficients set to $\kappa_{\mathrm{iso}} = 500 \, \mathrm{m^2 \, s^{-1}}$. The Gent–McWilliams scheme is implemented using the boundary value problem framework described by Ferrari et al. (2010). The Redi tensor changes to horizontal diffusion in regions of weak stratification, as described by Danabasoglu and McWilliams (1995). The vertical diffusivity is set to $2 \times 10^{-5} \, \mathrm{m^2 \, s^{-1}}$ in the interior, increasing to $10^{-2} \, \mathrm{m^2 \, s^{-1}}$ at the surface over a depth of 20 m to model the mixed layer. Each simulation was run for at least 3000 years, until equilibrium was reached.

In this paper, we compare two geometries, both with a long continent that extends from 70° to −52.5° and a short continent that extends from 70° to −21°. In the "standard" geometry the short continent is to the east of the narrow basin, and in the "exchanged" geometry the short continent is to the east of the wide basin. The exchanged geometry was initialized with sinking in the basin to the east of the short continent. Nonetheless, in both configurations sinking occurs in the basin to the west of the short continent, which, regardless of its width, represents the Atlantic. The other basin represents the Indo-Pacific. We choose these geometries because they have the same total MOC transport but different salinities in the north of the sinking basin despite longitudinally independent forcing.

As a measure of the overturning circulation, we use the zonally integrated residual overturning streamfunction (ROC; Wolfe and Cessi 2015), defined as

$$\psi(y, \tilde{b}) \equiv \frac{1}{T} \int_0^T \int_0^{L_x} \int_{-H}^0 v^\dagger \mathcal{H}[b(x, y, z, t) - \tilde{b}] \, dz \, dx \, dt, \quad (5)$$

where $v^\dagger$ is the Eulerian plus parameterized eddy velocity in the meridional direction, H is the total depth, L_x is the width of the basin, T is the averaging time scale (100 yr is chosen here), and $\mathcal{H}$ is the Heaviside function.
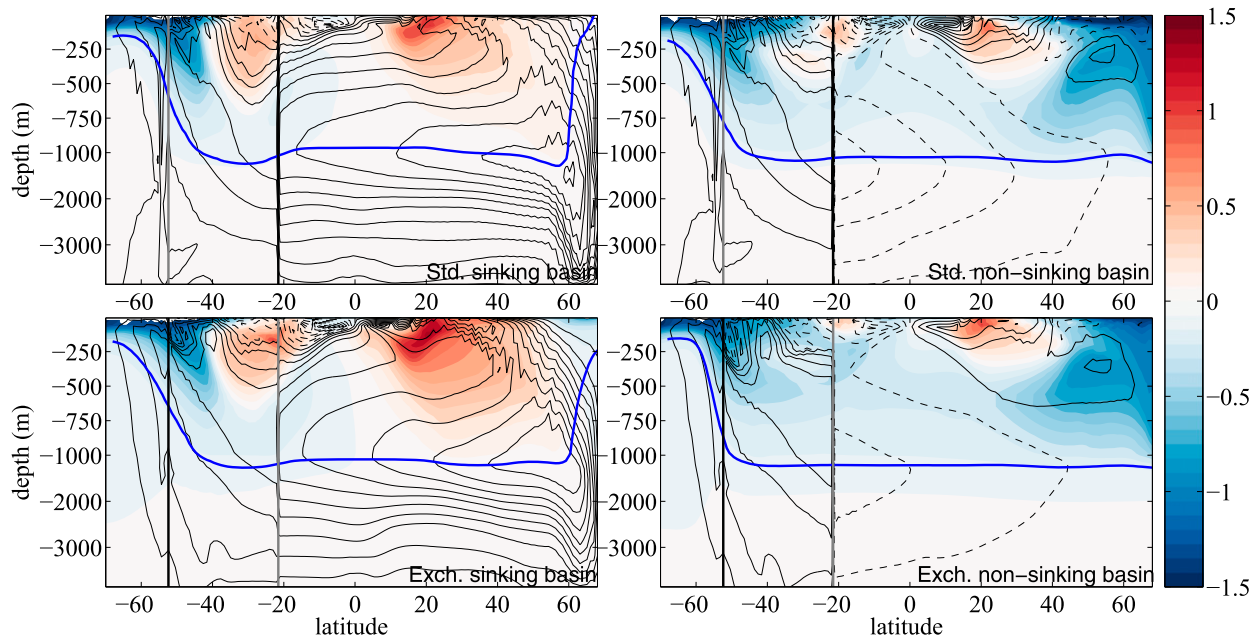
FIG. 2. The zonally averaged thickness-weighted salinity $\hat{S}$ (color shading; spacing 0.1) and the ROC ψ (black contours; spacing 2 Sv), in the (left) sinking basin and (right) nonsinking basin, of the (top) standard and (bottom) exchanged geometries; ψ and $\hat{S}$ are defined in Eqs. (5) and (6). Dashed lines represent negative values of ψ. The vertical black line denotes the end of the continent to the east of the narrow basin, and the vertical gray line denotes the end of the continent to the east of the wide basin. South of $-21°$, the zonal integral of ψ is over the whole width of the domain. The thick blue contour denotes the zonally averaged height of the isopycnal $b_m = 0.0066 \, \mathrm{m \, s^{-2}}$, which bounds the upper branch of the MOC from below.

The ROC streamfunction ψ denotes the zonally integrated transport of water above $b = \tilde{b}$.

$$\hat{S}(y,\tilde{b}) \equiv \frac{\frac{1}{T}\int_0^T \frac{1}{L_x}\int_0^{L_x}\int_{-H}^0 (S - S_{\mathrm{ref}})\delta[b(x,y,z,t) - \tilde{b}]\, dz\, dx\, dt}{\frac{1}{T}\int_0^T \frac{1}{L_x}\int_0^{L_x}\int_{-H}^0 \delta[b(x,y,z,t) - \tilde{b}]\, dz\, dx\, dt}. \tag{6}$$

The quantity $\hat{S}$ is zonally averaged at constant buoyancy, and therefore it can be contoured in the same panel as the ROC.

In Fig. 2, ψ (black contours) and $\hat{S}$ (filled color contours) are remapped into z coordinates using the zonal-mean isopycnal height, which is defined as

$$\mathcal{Z}(y,\tilde{b}) \equiv -\frac{1}{T}\int_0^T \frac{1}{L_x}\int_0^{L_x}\int_{-H}^0 \mathcal{H}[b(x,y,z,t) - \tilde{b}]\, dz\, dx\, dt. \tag{7}$$

Because of longitudinal buoyancy gradients, the zonally averaged remapping in Eq. (7) distorts the vertical extent of the mixed layer.

The isopycnal $b_m = 0.0066 \, \mathrm{m \, s^{-2}}$ (thick blue lines in Fig. 2) divides the upper and lower branches of the

The zonally averaged thickness-weighted salinity anomaly [as described in Young (2012)] is defined as

circulation: it passes close to the maximum of the ROC in both geometries. It is well known that heat and salt transports are defined up to a constant times the mass transport (Boccaletti et al. 2005). Here we define the advective component of salt transport as $v^\dagger(S - S_{\mathrm{ref}})$, because the volume-averaged salinity below the isopycnal b_m is very close to $S_{\mathrm{ref}} = 35$. This definition minimizes the advective salt transport below the isopycnal b_m. Below the isopycnal b_m, the salinity is approximately uniform (see Fig. 2); therefore with this definition almost all advective salt transport occurs above b_m.

Because the flow above $b_m = 0.0066 \, \mathrm{m \, s^{-2}}$ is horizontally divergent, it is not possible to describe it with a streamfunction. Instead, two pseudostreamfunctions of this flow are defined as

$$\chi_u(x, y) = -\frac{1}{T}\int_0^T \int_{-L}^y \int_{\zeta(x,\hat{y},b_m)}^0 u^\dagger(x,\hat{y},z,t)\,dz\,d\hat{y}\,dt \quad \text{and}$$
$$(8)$$

$$\chi_v(x, y) = \frac{1}{T}\int_0^T \int_0^x \int_{\zeta(x,\hat{y},b_m)}^0 v^\dagger(\hat{x},y,z,t)\,dz\,d\hat{x}\,dt + \chi_0(y),$$
$$(9)$$

where $\zeta(x, y, b_m)$ is the depth of isopycnal $b_m = 0.0066\,\mathrm{m\,s^{-2}}$ and $y = -L$ is the southern boundary of the domain. The function χ_0 is defined as

$$\chi_0(y) = \begin{cases} \chi_u(x = 0, y = y_c) & \text{for} \quad y > y_c, \\ \chi_u(x = 0, y) & \text{for} \quad y < y_c, \end{cases} \quad (10)$$

where $y = y_c$ is the end of the long continent: this choice of χ_0 allows the pseudostreamfunctions to be easily compared. Speich et al. (2001, 2002) use a pseudostreamfunction similar to χ_u (integrated above a depth level rather than a density level) to show the pathways of the warm route, the cold route, and the Tasman leakage in realistic-geometry ocean-only models.

Neither pseudostreamfunction describes the two-dimensional transport above b_m completely, but each pseudostreamfunction characterizes some aspects of the flow well. Above b_m and at the longitude of the short continent, the transport along open streamlines of χ_u is equivalent to the net zonal transport. Hence, χ_u more accurately describes the warm-route interbasin transport (Fig. 3). The residual transport along open streamlines of χ_v is equivalent to the net meridional transport above b_m at the southern edge of the sinking basin ($-21°$), which is itself equal to the warm-route interbasin transport plus the Ekman minus eddy transport into the sinking basin. Hence, χ_v more accurately describes the warm-route interbasin flow plus the Ekman minus eddy transport into the sinking basin (Fig. 4).

3. Components of salt transport

The top panel of Fig. 5 shows the salinity anomaly, vertically and zonally averaged above $b_m = 0.0066\,\mathrm{m\,s^{-2}}$. The "sinking region" is defined as the band of latitudes where the zonally integrated diapycnal velocity is negative and larger in magnitude than $5\,\mathrm{m^2\,s^{-1}}$. This region lies between $59°$ and $66°$ in the standard geometry and about $2°$ farther south in the exchanged geometry (see yellow and gray boxes in the top panel of Fig. 5).

In the sinking region, the zonally averaged salinity anomaly is higher for the standard geometry (see the red lines in the yellow and gray boxes in the top panel of Fig. 5), despite similar ROC transports in the Northern Hemisphere (see the red lines in the bottom panel of Fig. 5).
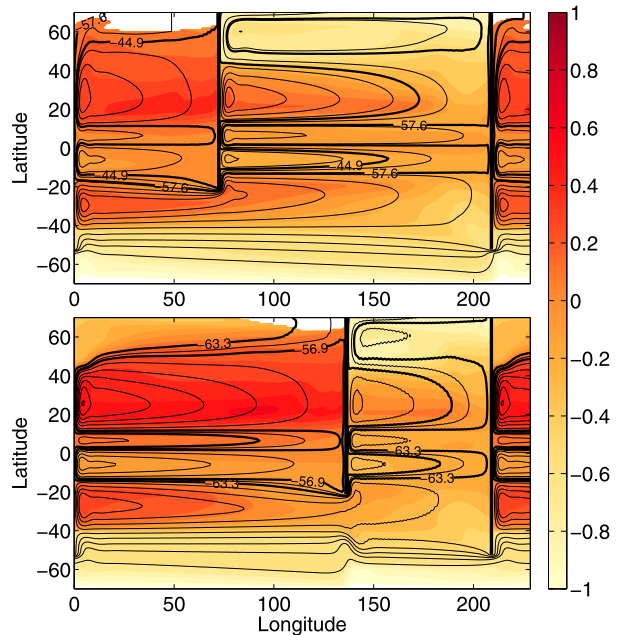

FIG. 3. Salinity anomaly, referenced to 35, vertically averaged above surface $b_m = 0.0066\,\mathrm{m\,s^{-2}}$ (color shading) and contours of pseudostreamfunction χ_u, as defined in Eq. (8) (black contours), for (top) the standard geometry and (bottom) the exchanged geometry. The thick black contours bound the region of open streamlines. These streamlines represent the warm-route interbasin flow. The transport along open streamlines is 12.7 Sv in the standard geometry and 6.4 Sv in the exchanged geometry. The isopycnal $b_m = 0.0066\,\mathrm{m\,s^{-2}}$ outcrops in the white area. The westernmost $20°$ of the domain is repeated on the right side of the panels.

Between the equator and $50°$, the zonally averaged salinity anomaly is higher for the exchanged geometry (see the red lines in the top panel of Fig. 5). Here, we will address how the components of salt transport produce the zonally averaged salinity distribution.

The difference in salinity between the two configurations can also be observed in the zonally averaged thickness-weighted salinity $\hat{S}$. In the sinking region, the salinity difference between configurations is very surface intensified (see the color contours north of $50°$ in the top left and bottom left panels of Fig. 2), and north of $60°$ the ROC streamfunction is much larger near the surface of the standard case (see the black contours in the top left and bottom left panels of Fig. 2). South of $50°$ in the sinking basin, the difference appears to be spread over the whole depth above b_m (see the color contours in the top left and bottom left panels of Fig. 2). However, at least some of the salinity difference at depth is caused by the deeper subtropical gyre in the sinking basin of the exchanged case, which is simply due to basin width and does not indicate any differences in the depth-integrated meridional salt transport p.u.w above b_m.
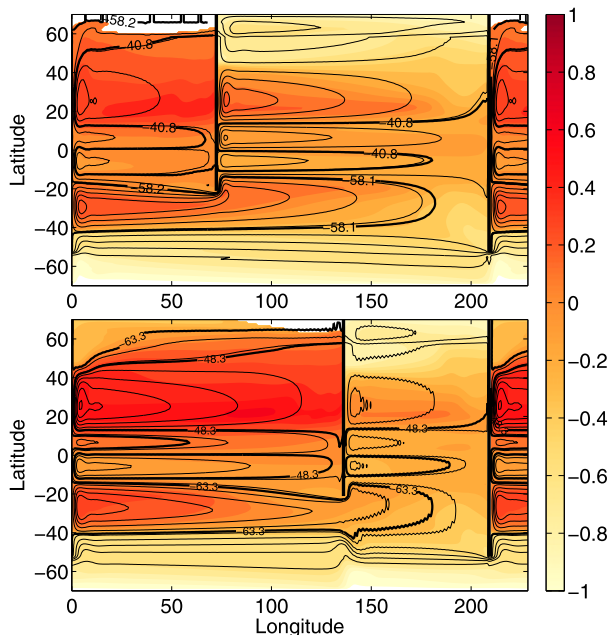
FIG. 4. Salinity anomaly, referenced to 35, vertically averaged above surface $b_m = 0.0066 \, \mathrm{m \, s^{-2}}$ (color shading) and contours of pseudostreamfunction χ_v, as defined in Eq. (9) (black contours) for (top) the standard geometry and (bottom) the exchanged geometry. The thick black contours bound the region of open streamlines. These streamlines represent the warm-route interbasin transport plus channel upwelling. The residual transport along open streamlines is 17.3 Sv in the standard geometry and 15 Sv in the exchanged geometry. The isopycnal $b_m = 0.0066 \, \mathrm{m \, s^{-2}}$ outcrops in the white area. The westernmost 20° of the domain is repeated on the right side of the panels.

FIG. 5. (top) Salinity anomaly, referenced to 35, depth and zonally averaged above $b_m = 0.0066 \, \mathrm{m \, s^{-2}}$ and across each basin, and (bottom) the residual transport above $b_m = 0.0066 \, \mathrm{m \, s^{-2}}$ in each basin. South of $-21°$, the zonal integral is taken across all longitudes. The yellow shading indicates the sinking region for the standard geometry, and the gray shading indicates the sinking region for the exchanged geometry. The black vertical line denotes the end of the short continent.

We divide the contours of χ_u and χ_v into open streamlines and closed streamlines, a partition that is often performed on 2D flows (see Childress and Gilbert 2008, ch. 5). For χ_u, so-called open streamlines are contours beginning in the nonsinking basin and ending in the sinking basin: these contours characterize the warm-route interbasin transport above b_m. The residual transport along these streamlines is 12.7 Sv (1 Sv $\equiv 10^6 \, \mathrm{m^3 \, s^{-1}}$) for the standard geometry and 6.4 Sv for the exchanged geometry. As described in Allison (2009) and Jones and Cessi (2016), conservation of buoyancy requires that the interbasin transport is equal to the Ekman minus eddy transport into the nonsinking basin plus the diapycnal upwelling in that basin. Because the Ekman, eddy, and diapycnal transport per unit width are approximately fixed, the strength of the interbasin transport is approximately proportional to the width of the nonsinking basin. The thick black lines in Fig. 3 bound the region of open streamlines of χ_u.

For χ_v, open streamlines are contours beginning in the Southern Hemisphere of the sinking basin, in the channel, or in the nonsinking basin and ending in the
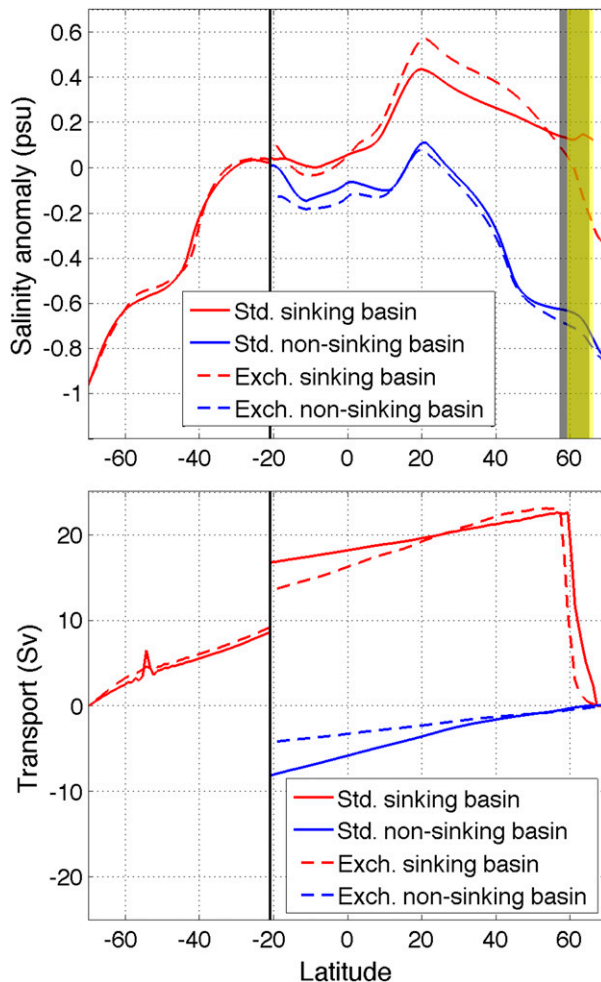
Northern Hemisphere of the sinking basin: these contours characterize the residual transport of the warm-route interbasin flow plus channel upwelling. The residual transport along these streamlines is 17.3 Sv for the standard geometry and 15 Sv for the exchanged geometry. The thick black lines in Fig. 4 bound the region of open streamlines of χ_v. Both descriptions show that all of the interbasin exchange occurs through the warm route.

To characterize the salt pathway into the north of the sinking basin, the total meridional salt transport above b_m, or G_{tot}, is decomposed into the following components: 1) the meridional advective transport in the area of open streamlines A_{open}, 2) the meridional diffusive transport in the area of open streamlines D_{open}, 3) the

meridional advective transport in the area of closed streamlines A_{closed}, and 4) the meridional diffusive transport in the area of closed streamlines D_{closed}. In summary we have

$$G_{\text{tot}}(y) = A_{\text{open}}(y) + D_{\text{open}}(y) + A_{\text{closed}}(y) + D_{\text{closed}}(y), \quad (11)$$

where

$$A_{\text{open}}(y) = \int_{\chi_w}^{\chi_e} \frac{1}{T} \int_0^T \int_{\zeta(b_m)}^0 v^\dagger (S - S_{\text{ref}}) \, dz \, dt \, dx, \quad (12)$$

$$D_{\text{open}}(y) = \int_{\chi_w}^{\chi_e} \frac{1}{T} \int_0^T \int_{\zeta(b_m)}^0 \kappa_{\text{iso}} \left(S_y - \frac{b_y}{b_z} S_z \right) dz \, dt \, dx, \quad (13)$$

$$A_{\text{closed}}(y) = \int_{x_w}^{x_e} \frac{1}{T} \int_0^T \int_{\zeta(b_m)}^0 v^\dagger (S - S_{\text{ref}}) \, dz \, dt \, dx \\ - A_{\text{open}}, \quad (14)$$

$$D_{\text{closed}}(y) = \int_{x_w}^{x_e} \frac{1}{T} \int_0^T \int_{\zeta(b_m)}^0 \kappa_{\text{iso}} \left(S_y - \frac{b_y}{b_z} S_z \right) dz \, dt \, dx \\ - D_{\text{open}}, \quad (15)$$

$\chi_{w,e}$ are the westernmost and easternmost open streamlines, $x_{w,e}$ are the western and eastern sides of the sinking basin, and κ_{iso} is the Redi coefficient.

The total salt transport p.u.w. above b_m, denoted by $G_{\text{tot}}/L_{n,w}$, is more relevant than G_{tot} for determining the salinity in the north of the sinking basin. North of $-21°$, $L_{n,w}(y)$ are the width of the narrow and wide basins respectively. South of $-21°$, $L_{n,w}(y)$ are equal to the width of the domain. The total salt transport p.u.w. above b_m is plotted for each basin of both configurations in Fig. 6a. In the sinking basin the salt transport p.u.w. is larger in the standard geometry than in the exchanged geometry (see the red lines north of $-21°$ in Fig. 6a). North of 40°, the difference between configurations widens (see the red lines at 50° in Fig. 6a). In the exchanged case, the lower salt transport p.u.w. reduces the salinity of the sinking region and increases the salinity at midlatitudes (see the red lines in the top panel of Fig. 5).

The black line in Fig. 6a represents the total salt transport p.u.w by the whole water column: in equilibrium this transport is determined by the surface freshwater flux. Extra northward salt transport in the upper branch of the MOC is balanced by extra southward salt transport in the lower branch, so in the sinking basin the southward salt transport below b_m is larger in the standard geometry (not shown).
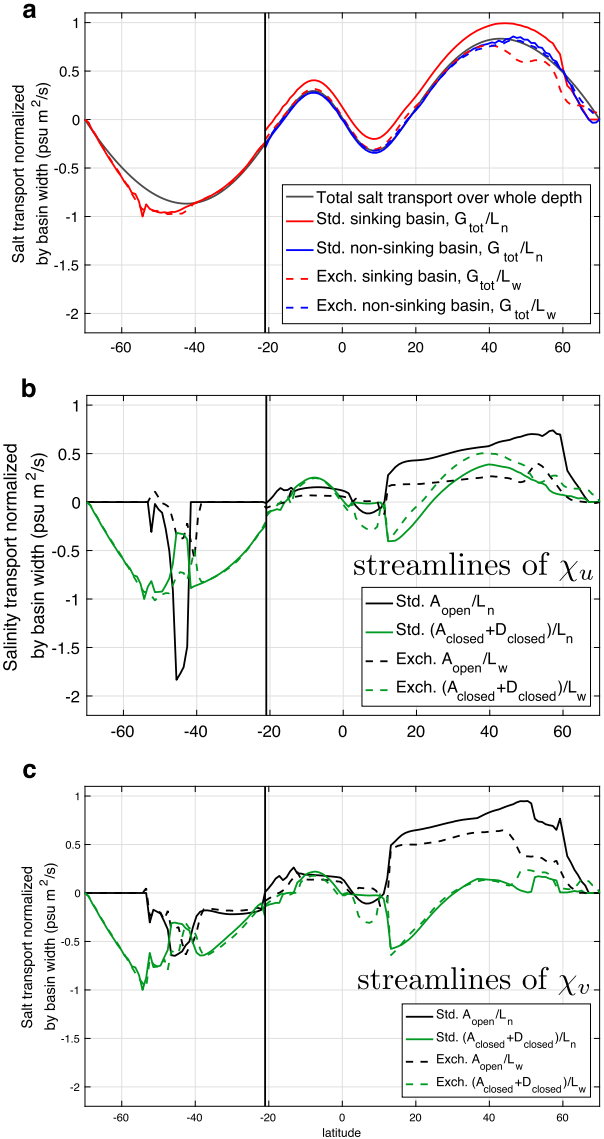

FIG. 6. (a) Total salt transport, vertically integrated over the whole water column (black curve) and vertically integrated above $b_m = 0.0066\,\text{m s}^{-2}$ (red and blue curves), zonally averaged across each basin north of $-21°$; south of $-21°$, the zonal integral is taken across all longitudes. (b) The advective salt transport for χ_u (black curves) and the salt transport for streamlines of χ_u (green curves) in the sinking basin north of $-21°$ (normalized by the basin width for ease of comparison) and in the whole domain south of $-21°$ (normalized by the domain width for ease of comparison). (c) The advective salt transport for streamlines of χ_v (black curves) and the salt transport for χ_v (green curves), in the sinking basin north of $-21°$ (normalized by the basin width for ease of comparison) and in the whole domain south of $-21°$ (normalized by the domain width for ease of comparison). The quantities are defined in Eqs. (11)–(15). Here, $L_n(y)$ denotes the width of the narrow basin for $y \geq y_c$ and the width of the domain for $y < y_c$; $L_w(y)$ denotes the width of the wide basin for $y \geq y_c$ and the width of the domain for $y < y_c$.

In the nonsinking basin the salt transport p.u.w. in the upper branch is independent of geometry (see the blue lines in Fig. 6a) and very similar to the salt transport p.u.w. in the whole water column (see the black line in Fig. 6a). This leads to similar salinities in the nonsinking basin of both geometries (see the blue lines in the top panel of Fig. 5). Henceforth we will focus on the salt transport in the sinking basin, which is different between configurations.

Figure 6b shows the meridional advective salt transport in the area of open streamlines of χ_u, $A_{open}/L_{n,w}$, (black lines) and the meridional salt transport in the area of closed streamlines of χ_u, $(A_{closed} + D_{closed})/L_{n,w}$ (green lines) in the sinking basin, both normalized by basin width for ease of comparison. Figure 6c shows the same salt transports, but for streamlines of χ_v. The diffusive component in the area of open streamlines (D_{open}) is not shown because it is negligible. Because the streamlines of χ_u and χ_v are depth and time averaged, salt can be advected across them by the baroclinic component of the flow if the velocity and salinity are correlated in the vertical direction.[1] The meridional salt transport in the area of open streamlines is well approximated with the meridional salt transport by the vertically and zonally integrated velocity above b_m in the region of open streamlines (see the appendix for details).

At most latitudes north of $-21°$, the salt transport p.u.w. in the area of open streamlines, $A_{open}/L_{n,w}$, is larger in the standard case than in the exchanged case for both χ_u and χ_v (see the black lines in Figs. 6b,c). This indicates that in the standard configuration the higher total salt transport p.u.w. is effected by the larger warm-route interbasin transport (the difference between the red lines in Fig. 6a is similar to the difference between the black lines in Fig. 6b). The larger salt transport p.u.w. north of $-21°$ increases the vertically and zonally averaged salinity above b_m north of $60°$ (see the red lines in the top panel of Fig. 5). Thus, it is likely that strengthening the warm-route transport would increase the salinity in the north of the sinking basin.

In the narrow basin's subtropical gyre western boundary current, salinity is approximately independent of latitude. Hence, A_{open} is approximately constant between $18°$ and $45°$ for both χ_u and χ_v. In this region $L_{n,w}$ decreases with latitude, so $A_{open}/L_{n,w}$ increases with latitude (black lines in Figs. 6b,c). The zero crossings of $(A_{closed} + D_{closed})/L_{n,w}$ occur at the northern and southern edge of each gyre, where the salt transport is all performed by the open streamlines because the area of closed streamlines is very narrow (green lines in Figs. 6b,c).

In the basins, the Ekman transport is returned in a western boundary current, so it is part of the closed-streamline residual transport. The salt transport in the area of closed streamlines appears to be dominated by the Ekman transport of salt. This transport carries salt away from regions of high evaporation (e.g., the peak evaporation minus precipitation at about $20°$) and into areas of high precipitation (green lines in Figs. 6b,c). The Ekman transport p.u.w., and hence the salt transport p.u.w. in the area of closed streamlines, is very similar between geometries (see the green lines in Figs. 6b,c).

4. Causes of larger northward salt transport in the standard case

At $-21°$ in the sinking basin, there is a larger northward salt transport in the standard geometry than in the exchanged geometry (see the red lines in Fig. 6a). In the nonsinking basin, the southward residual transport between open streamlines is larger in the standard geometry than in the exchanged geometry (cf. open streamlines in the top and bottom panels of Figs. 3 and 4). Hence, in the nonsinking basin, more salt is advected southward in the standard geometry, increasing the salinity directly south of the short continent (not shown). This higher salinity south of the short continent is advected into the sinking basin by the flow along open streamlines, causing a larger northward salt transport at $-21°$.

In addition, for the exchanged case, there is a drop in the northward salt transport p.u.w. in the sinking basin, going from $40°$ to $50°$. This drop is less prominent in the standard case (see the red lines in Fig. 6a). For pseudostreamfunction χ_v,[2] the open-streamline salt transport p.u.w. in the exchanged configuration also shows this drop (see the black lines in Fig. 6c). The aim of this section is to understand why the salt transport p.u.w decreases between $40°$ and $50°$ in the exchanged configuration: in this latitude band, salt must be lost from the region of open streamlines more efficiently than in the standard configuration.

The following budget describes the components of the flow into and out of the area of open streamlines between $40°$ and $50°$ (outlined in green in Fig. 7), depth integrated above b_m. The black dashed lines in Fig. 7 represent the easternmost and westernmost open streamlines.

---

[1] If the flow were entirely barotropic (i.e., 2D) above b_m, the advective transport across a closed streamline would be zero.

[2] The results in this section are for pseudostreamfunction χ_v. Using the pseudostreamfunction χ_u gives the same qualitative differences between the standard configuration and the exchanged configuration.
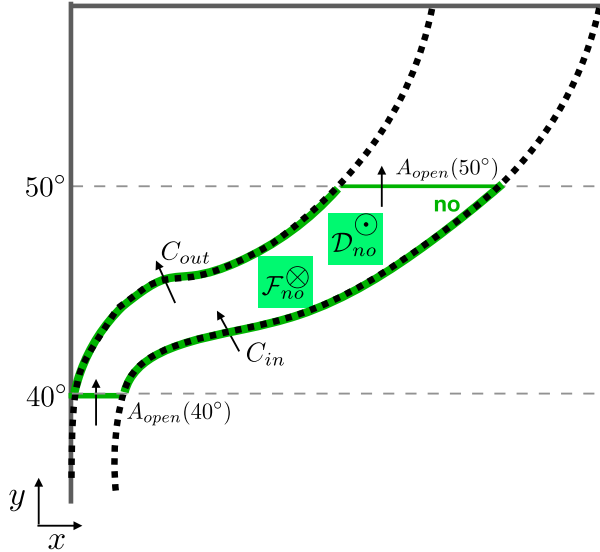
FIG. 7. Schematic of salt transport into the region of open streamlines between 40° and 50°. The solid gray lines represent the boundaries of the domain, and the black dotted lines represent the easternmost and westernmost open streamlines; C_{in} is the horizontal cross-streamline salt transport above the isopycnal b_m into the region of open streamlines (the area bounded by green lines) from the south, $\mathcal{F}_{\text{no}}$ is the salt transport into the region of open streamlines at the surface, $\mathcal{D}_{\text{no}}$ is the diapycnal salt transport across b_m into the region of open streamlines, C_{out} is the horizontal cross-streamline salt transport above the isopycnal b_m out of the region of open streamlines into the north, and A_{open} is the meridional salt transport in the region of open streamlines.

Assuming the model is in a steady state, conservation of salt in each region gives

$$\mathcal{F}_{\text{no}} + \mathcal{D}_{\text{no}} - C_{\text{out}} + C_{\text{in}} + A_{\text{open}}(40°) - A_{\text{open}}(50°) = 0, \tag{16}$$

where $\mathcal{F}_{\text{no}}$ is the area-integrated salt transport at the surface, $\mathcal{D}_{\text{no}}$ is the area-integrated diapycnal salt transport across b_m, C_{in} is the salt transport into the region across the easternmost open streamline and C_{out} is the salt transport out of the region across the westernmost open streamline. Area integrals are over the region of open streamlines between 40° and 50°. Table 1 gives the value of each term in both configurations. All salt transports are normalized by the basin width at 40° for ease of comparison.

In the standard case, the cross-streamline salt transports C_{in} and C_{out}, the area-integrated surface salt flux $\mathcal{F}_{\text{no}}$, and the area-integrated diapycnal flux $\mathcal{D}_{\text{no}}$ are all an order of magnitude smaller than the along-streamline salt transport as measured by A_{open}. Therefore the advective salt transports at 40° and 50° are very similar (solid black line in Fig. 6c). In the exchanged case, the salt transport across the easternmost open streamline,

TABLE 1. Salt transport budget for the open streamline region of streamfunction χ_v between 40° and 50° in the sinking basin. Figure 7 shows a schematic of this region. The salt transports are normalized by the basin width at 40°: $L_{n,w}(40°)$.

Parameter	Standard case ($m^2\,s^{-1}$)	Exchanged case ($m^2\,s^{-1}$)
$C_{\text{out}}/L_{n,w}(40°)$	0.0090	0.032
$\mathcal{F}_{\text{no}}/L_{n,w}(40°)$	-0.013	-0.038
$\mathcal{D}_{\text{no}}/L_{n,w}(40°)$	0.018	-0.022
$C_{\text{in}}/L_{n,w}(40°)$	0.044	-0.23
$A_{\text{open}}(40°)/L_{n,w}(40°)$	0.84	0.61
$A_{\text{open}}(50°)/L_{n,w}(40°)$	0.80	0.29

C_{in}, is more negative, and $A_{\text{open}}(50°) \approx A_{\text{open}}(40°) + C_{\text{in}}$. The meridional salt transport along open streamlines in the exchanged case is smaller at 50° (dashed black line in Fig. 6c) because some salt is transported southward into the subtropical gyre.

The salt transport across the easternmost open streamline C_{in} is dominated by southward advection of salt in the Ekman layer. In the exchanged case, the easternmost open streamline turns eastward at a lower latitude than in the standard case (cf. the thick black contour marked 40.8 in the top panel of Fig. 4 with the thick black contour marked 48.3 in the bottom panel of Fig. 4). The subpolar gyre western boundary current, which is stronger in a wider basin (Jones and Cessi 2017), forces the open streamlines to turn away from the boundary earlier in the exchanged case. Between 40° and 50°, the Ekman transport is southward, perpendicular to the easternmost open streamline in the exchanged configuration (thick black contour marked -48.3 in the bottom panel of Fig. 4), but not in the standard configuration (thick black contour marked -40.8 in the top panel of Fig. 4). Thus, between 40° and 50°, the southward cross-streamline Ekman transport of salt is smaller in the standard configuration.

The normalized cross-streamline salt transport $C_{\text{in}}/L_w(40°)$ freshens the open-streamline flow between 40° and 50° in the sinking basin of the exchanged configuration, reducing the northward along-streamline salt transport. This intensifies the gradients of zonally averaged salinity above b_m (as shown by the red dashed line in the top panel of Fig. 5). North of 60°, the fresher surface in the sinking basin of the exchanged case pushes the ROC streamfunction below about 200-m depth (black contours in the bottom left panel of Fig. 2).

5. Summary and discussion

In this paper, we study the transport of salt in an idealized global ocean model consisting of two basins of different widths connected by a re-entrant channel.

We compare two versions of this model, one with the short continent to the east of the narrow basin (the standard geometry) and one with the short continent to the east of the wide basin (the exchanged geometry). Deep water is formed in the basin to the west of the short continent in both configurations. The interbasin transport flows westward south of the short continent (through the warm route) and it has twice the strength in the standard geometry as in the exchanged geometry. We define two different pseudostreamfunctions: one in which the open streamlines represent the warm-route interbasin transport and one in which the open streamlines represent the warm-route interbasin transport plus the channel upwelling. Neither of these transport representations shows a cold route pathway. We divide the salt transport entering the sinking basin above a mid-depth isopycnal into the salt transport by flow along open streamlines and the salt transport in the area of closed streamlines. This method gives an approximation of the net salt transport between basins. The salt transport between basins is otherwise difficult to obtain, because it is difficult to separate the interbasin exchange flow (which is on the order of 5 Sv) from the ACC (which is on the order of 40 Sv above b_m).

In the sinking basin, the northward salt transport per unit width is larger in the standard configuration than in the exchanged configuration. In the standard configuration, the warm-route interbasin transport carries salt southward more efficiently in the nonsinking basin and northward more efficiently in the sinking basin, leading to higher salinity in the north of the sinking basin. In the exchanged configuration, the wider sinking basin leads to a larger salt transport out of the region of open streamlines at about 40°, consistent with Jones and Cessi (2017). This salt transport out of the region of open streamlines also reduces salinity in the north of the sinking basin in the exchanged case.

This study suggests that the total salt transport from the Indo-Pacific to the Atlantic is primarily effected by the interbasin exchange associated with the ITF and the Tasman leakage, rather than by the gyral flow. Increasing the interbasin transport is likely effective at raising the salinity of the North Atlantic. Higher salinity could act to stabilize the MOC, which is enabled by high surface densities in the North Atlantic. The strength of the Agulhas leakage, which is fed by the ITF and Tasman leakage, responds to upstream conditions (van Sebille et al. 2009) and to changes in the Southern Hemisphere westerlies (Gordon 1986; Biastoch et al. 2009). If variations in the strength of the Agulhas leakage are associated with variations in salt (and heat) transport, they may drive MOC variability. In particular, climate models predict that Southern Hemisphere

westerlies will move southward and intensify over the next century, leading to an increase in the Agulhas leakage on decadal time scales (Biastoch and Böning 2013), and to larger northward salt transport by the warm route.

APPENDIX

Salt Advection by the Velocity, Vertically Integrated above b_m and Zonally Integrated in the Area of Open Streamlines

In this paper, we assume that the vertically and zonally averaged salt transport in the area of open streamlines A_{open} is approximately equal to the vertically and zonally averaged salt transport by the vertically and zonally integrated along-streamline flow. This is equivalent to assuming that the salt transport by the vertically and zonally integrated flow above b_m in the area of open streamlines is much larger than the salt transport by the baroclinic component of the flow above b_m, or by zonal variations of the depth-averaged velocity in this area. To confirm our assumption, we decompose A_{open} into 1) the salt advection by the vertically and zonally averaged meridional velocity above b_m between open streamlines and 2) a residual due to correlations between salinity and velocity in the vertical and zonal directions. This gives

$$A_{\text{open}}(y) = X_{\text{open}}(y)S_{\text{open}}(y) + A_{\text{open}}^{(\text{res})}(y) \qquad (\text{A1})$$

$$= \left[\int_{\chi_w}^{\chi_e} \int_{\zeta(b_m)}^{0} v^\dagger \, dz \, dx \right] \left[\frac{\int_{\chi_w}^{\chi_e} \int_{\zeta(b_m)}^{0} (S - S_{\text{ref}}) \, dz \, dx}{\int_{\chi_w}^{\chi_e} \int_{\zeta(b_m)}^{0} dz \, dx} \right]$$

$$+ A_{\text{open}}^{(\text{res})}, \qquad (\text{A2})$$

where X_{open} is the meridional residual transport along open streamlines above b_m, S_{open} is the zonally and vertically averaged salinity in the area of open streamlines above b_m, and $A_{\text{open}}^{(\text{res})}$ is the remaining meridional salt transport in the area of open streamlines above b_m.

The salt transport, $X_{\text{open}}S_{\text{open}}$, normalized by the basin width, is shown in Fig. A1. North of $-21°$, most of the salt advection p.u.w. in the region of open streamlines
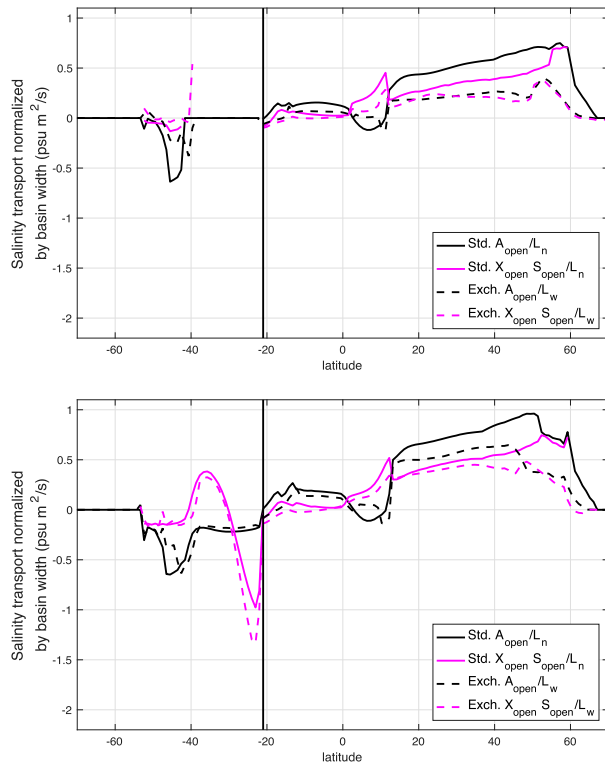
FIG. A1. The advective salt transport (black lines) and $X_{\text{open}}S_{\text{open}}$ (pink lines) in the sinking basin north of $-21°$ (normalized by the basin width for ease of comparison) and in the whole domain south of $-21°$ (normalized by the domain width for ease of comparison) for streamlines (top) χ_u and (bottom) χ_v. The black vertical line denotes the end of the short continent. Here, $L_n(y)$ denotes the width of the narrow basin for $y \geq y_c$ and the width of the domain for $y < y_c$; $L_w(y)$ denotes the width of the wide basin for $y \geq y_c$ and the width of the domain for $y < y_c$.

A_{open} is explained by the vertically and zonally averaged meridional velocity above b_m and between open streamlines $X_{\text{open}}S_{\text{open}}$ (cf. black and pink lines in Fig. A1). The salt transport in the region of open streamlines A_{open} is well approximated with the meridional advection by the vertically and zonally integrated velocity in that region. Variations in S_{open} dominate the term $X_{\text{open}}S_{\text{open}}$. At $-21°$, S_{open} is larger in the standard geometry, producing greater advective salt transport $A_{\text{open}}(-21°)$ in the standard geometry.

REFERENCES

Allison, L. C., 2009: Spin-up and adjustment of the Antarctic Circumpolar Current and global pycnocline. Ph.D. thesis, University of Reading, 207 pp.

Biastoch, A., and C. W. Böning, 2013: Anthropogenic impact on Agulhas leakage. *Geophys. Res. Lett.*, **40**, 1138–1143, https://doi.org/10.1002/grl.50243.

——, ——, F. U. Schwarzkopf, and J. Lutjeharms, 2009: Increase in Agulhas leakage due to poleward shift of Southern Hemisphere westerlies. *Nature*, **462**, 495–498, https://doi.org/10.1038/nature08519.

Boccaletti, G., R. Ferrari, A. Adcroft, D. Ferreira, and J. Marshall, 2005: The vertical structure of ocean heat transport. *Geophys. Res. Lett.*, **32**, L10603, https://doi.org/10.1029/2005GL022474.

Cessi, P., and C. S. Jones, 2017: Warm-route versus cold-route interbasin exchange in the meridional overturning circulation. *J. Phys. Oceanogr.*, **47**, 1981–1997, https://doi.org/10.1175/JPO-D-16-0249.1.

Childress, S., and A. D. Gilbert, 2008: Magnetic structure in steady integrable flows. *Stretch, Twist, Fold: The Fast Dynamo*, Springer Science & Business Media, 124–127.

Danabasoglu, G., and J. C. McWilliams, 1995: Sensitivity of the global ocean circulation to parameterizations of mesoscale tracer transports. *J. Climate*, **8**, 2967–2987, https://doi.org/10.1175/1520-0442(1995)008<2967:SOTGOC>2.0.CO;2.

Ferrari, R., S. M. Griffies, A. J. G. Nurser, and G. K. Vallis, 2010: A boundary-value problem for the parameterized mesoscale eddy transport. *Ocean Modell.*, **32**, 143–156, https://doi.org/10.1016/j.ocemod.2010.01.004.

Garzoli, S. L., M. O. Baringer, S. Dong, R. C. Perez, and Q. Yao, 2013: South Atlantic meridional fluxes. *Deep-Sea Res. I*, **71**, 21–32, https://doi.org/10.1016/j.dsr.2012.09.003.

Gent, P. R., and J. C. McWilliams, 1990: Isopycnal mixing in ocean circulation models. *J. Phys. Oceanogr.*, **20**, 150–155, https://doi.org/10.1175/1520-0485(1990)020<0150:IMIOCM>2.0.CO;2.

Gordon, A. L., 1985: Indian-Atlantic transfer of thermocline water at the Agulhas retroflection. *Science*, **227**, 1030–1034, https://doi.org/10.1126/science.227.4690.1030.

——, 1986: Interocean exchange of thermocline water. *J. Geophys. Res.*, **91**, 5037–5046, https://doi.org/10.1029/JC091iC04p05037.

Jones, C. S., and P. Cessi, 2016: Interbasin transport of the meridional overturning circulation. *J. Phys. Oceanogr.*, **46**, 1157–1169, https://doi.org/10.1175/JPO-D-15-0197.1.

——, and ——, 2017: Size matters: Another reason why the Atlantic is saltier than the Pacific. *J. Phys. Oceanogr.*, **47**, 2843–2859, https://doi.org/10.1175/JPO-D-17-0075.1.

Lumpkin, R., and K. Speer, 2007: Global ocean meridional overturning. *J. Phys. Oceanogr.*, **37**, 2550–2562, https://doi.org/10.1175/JPO3130.1.

Marshall, J., A. Adcroft, C. Hill, L. Perelman, and C. Heisey, 1997a: A finite-volume, incompressible Navier Stokes model for studies of the ocean on parallel computers. *J. Geophys. Res.*, **102**, 5753–5766, https://doi.org/10.1029/96JC02775.

——, C. Hill, L. Perelman, and A. Adcroft, 1997b: Hydrostatic, quasi-hydrostatic, and nonhydrostatic ocean modeling. *J. Geophys. Res.*, **102**, 5733–5752, https://doi.org/10.1029/96JC02776.

Nilsson, J., P. L. Langen, D. Ferreira, and J. Marshall, 2013: Ocean basin geometry and the salinification of the Atlantic Ocean. *J. Climate*, **26**, 6163–6184, https://doi.org/10.1175/JCLI-D-12-00358.1.

Rahmstorf, S., 1996: On the freshwater forcing and transport of the Atlantic thermohaline circulation. *Climate Dyn.*, **12**, 799–811, https://doi.org/10.1007/s003820050144.

Redi, M. H., 1982: Oceanic isopycnal mixing by coordinate rotation. *J. Phys. Oceanogr.*, **12**, 1154–1158, https://doi.org/10.1175/1520-0485(1982)012<1154:OIMBCR>2.0.CO;2.

Reid, J. L., 1961: On the temperature, salinity, and density differences between the Atlantic and Pacific Oceans in the upper kilometre. *Deep-Sea Res.*, **7**, 265–275, https://doi.org/10.1016/0146-6313(61)90044-2.

Ridgway, K. R., and J. R. Dunn, 2007: Observational evidence for a Southern Hemisphere oceanic supergyre. *Geophys. Res. Lett.*, **34**, L13612, https://doi.org/10.1029/2007GL030392.

Rintoul, S. R., 1991: South Atlantic interbasin exchange. *J. Geophys. Res. Oceans*, **96**, 2675–2692, https://doi.org/10.1029/90JC02422.

Speich, S., B. Blanke, and G. Madec, 2001: Warm and cold water routes of an O.G.C.M. thermohaline conveyor belt. *Geophys. Res. Lett.*, **28**, 311–314, https://doi.org/10.1029/2000GL011748.

——, ——, P. de Vries, S. Drijfhout, K. Döös, A. Ganachaud, and R. Marsh, 2002: Tasman leakage: A new route in the global ocean conveyor belt. *Geophys. Res. Lett.*, **29**, 1416, https://doi.org/10.1029/2001GL014586.

van Sebille, E., A. Biastoch, P. J. van Leeuwen, and W. P. M. de Ruijter, 2009: A weaker Agulhas Current leads to more Agulhas leakage. *Geophys. Res. Lett.*, **36**, L03601, https://doi.org/10.1029/2008GL036614.

Wolfe, C. L., and P. Cessi, 2015: Multiple regimes and low-frequency variability in the quasi-adiabatic overturning circulation. *J. Phys. Oceanogr.*, **45**, 1690–1708, https://doi.org/10.1175/JPO-D-14-0095.1.

Young, W. R., 2012: An exact thickness-weighted average formulation of the Boussinesq equations. *J. Phys. Oceanogr.*, **42**, 692–707, https://doi.org/10.1175/JPO-D-11-0102.1.